ADVANCED MATERIALS
www.advmat.de

Physical Origin of Negative Differential Resistance in V_3O_5 and Its Application as a Solid-State Oscillator

Sujan Kumar Das, Sanjoy Kumar Nandi, Camilo Verbel Marquez, Armando Rúa, Mutsunori Uenuma, Etienne Puyoo, Shimul Kanti Nath, David Albertini, Nicolas Baboux, Teng Lu, Yun Liu, Tobias Haeger, Ralf Heiderhoff, Thomas Riedl, Thomas Ratcliff, and Robert Glen Elliman*

Oxides that exhibit an insulator–metal transition can be used to fabricate energy-efficient relaxation oscillators for use in hardware-based neural networks but there are very few oxides with transition temperatures above room temperature. Here the structural, electrical, and thermal properties of V_3O_5 thin films and their application as the functional oxide in metal/oxide/metal relaxation oscillators are reported. The V_3O_5 devices show electroforming-free volatile threshold switching and negative differential resistance (NDR) with stable (<3% variation) cycle-to-cycle operation. The physical mechanisms underpinning these characteristics are investigated using a combination of electrical measurements, in situ thermal imaging, and device modeling. This shows that conduction is confined to a narrow filamentary path due to self-confinement of the current distribution and that the NDR response is initiated at temperatures well below the insulator–metal transition temperature where it is dominated by the temperature-dependent conductivity of the insulating phase. Finally, the dynamics of individual and coupled V_3O_5-based relaxation oscillators is reported, showing that capacitively coupled devices exhibit rich non-linear dynamics, including frequency and phase synchronization. These results establish V_3O_5 as a new functional material for volatile threshold switching and advance the development of robust solid-state neurons for neuromorphic computing.

1. Introduction

Devices that exhibit threshold switching, or current-controlled negative differential resistance (NDR), are of interest as selector elements in non-volatile memory cross-point arrays, where they can be employed to reduce sneak currents, and as neurons in neuromorphic computing networks.[1] Their application in hardware-based neuromorphic computing is based on the fact that the NDR response can be used to fabricate compact relaxation oscillators.[2] These can then be coupled in pairs to emulate the spiking response of biological neurons in a Spiking Neural Network[3] or integrated in arrays with coupling resistors or capacitors serving as network weights, to define an oscillatory neural network.[4]

Oscillators based on simple, two-terminal metal/oxide/metal (MOM) structures offer many advantages for such applications, including simple structure,

S. K. Das, S. K. Nandi, S. K. Nath, T. Ratcliff, R. G. Elliman
Research School of Physics
The Australian National University
Canberra, ACT 2601, Australia
E-mail: sanjoy.nandi@anu.edu.au

S. K. Das
Department of Physics
Jahangirnagar University
Dhaka 1342, Bangladesh

C. V. Marquez, A. Rúa
Department of Physics
University of Puerto Rico
Mayaguez, PR 00681, USA

The ORCID identification number(s) for the author(s) of this article can be found under https://doi.org/10.1002/adma.202208477.

DOI: 10.1002/adma.202208477

M. Uenuma
Information Device Science Laboratory
Nara Institute of Science and Technology (NAIST)
Nara 630-0192, Japan

E. Puyoo, D. Albertini, N. Baboux
Université Lyon
INSA Lyon
CNRS
Ecole Centrale de Lyon
Université Claude Bernard Lyon 1, CPE Lyon, INL, UMR5270,
Villeurbanne 69621, France

S. K. Nath
Department of Electrical, Electronic and Computer Engineering
The University of Western Australia
Crawley, WA 6009, Australia

T. Lu, Y. Liu
Research School of Chemistry
The Australian National University
Canberra, ACT 2601, Australia

T. Haeger, R. Heiderhoff, T. Riedl
Institute of Electronic Devices
Wuppertal Center for Smart Materials & Systems
University of Wuppertal
Rainer-Gruenter-Strasse 21, 42119 Wuppertal, Germany

scalability, and complementary metal–oxide–semiconductor (CMOS) compatibility, but existing devices are often limited by the physical properties of the functional oxide layer.[3c] In principle, the only requirement for NDR is that the oxide conductivity increases super-linearly with temperature, which is true for most binary metal-oxides.[5] However, in practice, the device response is often dominated by other processes, such as non-volatile resistive switching or permanent dielectric breakdown due to defect generation and migration.[6] As a consequence, only a few oxides exhibit reliable NDR.[1c,2b,7,8]

Materials that exhibit a thermally induced insulator–metal transition (IMT) are of particular interest for neuromorphic computing as large conductivity changes can be achieved with small variations in temperature thereby enabling power-efficient operation. Vanadium dioxide (VO_2) has received particular attention in this regard due to its low temperature (≈340 K) thermally induced insulator–metal transition.[9] For example, Yi et al.[2b] showed that both resistively and capacitively coupled VO_2 oscillators were capable of emulating 23 distinct biological neuron spiking characteristics. However, despite its impressive performance, VO_2 has two major limitations: its IMT temperature ($T_{IMT} \approx 340$ K) is below the typical operating temperature (400 K) of modern computers,[10] and devices have poor endurance due to the damage caused by large volume changes during the IMT.[11] Attempts have been made to address these issues, including the use of doping and alloying to increase the IMT temperature or induce field-driven switching, but so far these attempts have had only limited success.[12] An alternative is to use a material with a higher IMT temperature, but few suitable alternatives exist with a critical temperature $T_{IMT} >$ 400 K. NbO_2 is one possible candidate ($T_{IMT} \approx 1070$ K) but its transition temperature is so high that the IMT plays little role in its switching response. Another little explored possibility is V_3O_5.[13]

V_3O_5 is a Magnéli phase of vanadium oxide that undergoes a thermally induced IMT at ≈420 K, during which its resistivity decreases by approximately one order of magnitude.[13] The IMT has been attributed to a change in the arrangement of V^{3+} and V^{4+} ions from an ordered to a disordered distribution and a concomitant reduction in the unit cell size by ≈0.14% which leads to band overlap, giving rise to the metallic phase.[14] Although the phase transition in V_3O_5 was first reported nearly five decades ago, it has received limited attention due to the challenges associated with the synthesis of V_3O_5 films. Vanadium is a multivalent ion and the oxygen stoichiometry must be accurately controlled to produce high-quality, crystalline V_3O_5-thin films[15]. However, recent advances in thin-film deposition and characterization have yielded routine preparation methods for V_3O_5 based on reactive sputter deposition[16] or controlled oxygen evolution.[16b]

Fisher et al.[17] first demonstrated the NDR characteristics in V_3O_5-based devices. However, that study remains controversial as the devices required an electroforming step that can create the VO_2 phase within the film and contribute to the observed switching behavior.[9b] A more recent study by Adda et al.[13] provided important insight into the threshold-switching mechanism V_3O_5 and its potential as a functional oxide for oscillator-based neuromorphic computing.

This study combines structural, electrical, and thermal characterization of V_3O_5 films with in situ thermal imaging and modeling of lateral metal/oxide/metal device structures to extend the understanding of threshold switching and negative differential resistance in V_3O_5-based devices, and further explores the dynamics of V_3O_5-based oscillators and their coupling dynamics. These results establish V_3O_5 as an interesting new material for low-power, oxide-based analog computing applications, including oscillator-based neuromorphic computing.

2. Results and Discussion

2.1. Physical Properties of V_3O_5 Thin Film

Figure 1a shows a grazing-incidence X-ray diffraction (GI-XRD) spectrum of an as-deposited V_3O_5 film on a SiO_2 substrate. Rietveld refinement analysis confirms that the dominant peaks are consistent with the (200), (002), (−112), (310) and (−213) planes of monoclinic V_3O_5, which has a structure with the $P_{2/c}$ space group (JCPDS card 72–0977).[18] Room-temperature, high-resolution X-ray photoelectron spectroscopy (XPS) analysis (see Supporting Information) shows that the V2p core level can be deconvoluted into V^{4+} and V^{3+} states, consistent with a previously reported XPS study of V_3O_5 thin films.[19] The estimated ion fractions calculated from fitted V^{4+} and V^{3+} XPS peaks are 3.61% and 7.28%, respectively, which is equivalent to an average oxidation state of 3.33, matching the theoretical value for V_3O_5 ($V^{3.33+}$).[19]

The resistivity of the V_3O_5 thin film was measured as a function of temperature using four-point contacts in a van der Pauw configuration. The measurements were performed over the temperature range of 300–500 K during heating and cooling cycles and are summarized in Figure 1b. The resistivity is observed to decrease monotonically with increasing temperature, falling by approximately an order of magnitude between room temperature and the onset of the IMT, and by a further order of magnitude at 420 ± 5 K as it undergoes the insulator-metal transition.[14a] The broad temperature range for the IMT is attributed to the inhomogeneous nature of the V_3O_5 phase transition, which is evident from the C-AFM maps of through-film current distributions shown in Figure 1c,d. Well below the transition temperature the film is in its insulating state and conduction is dominated by only a few isolated grains but as it is heated near the transition temperature, the number of conductive grains increases rapidly but still with considerable dispersion in their conductivities.[20]

Figure 1e shows the thermal conductivity of a V_3O_5 thin film as a function of temperature, as measured by scanning near-field thermal microscopy (SThM) using the 3ω-technique.[21] The thermal conductivity of the insulation phase increases monotonously from 0.57 to 0.76 W m^{-1} K^{-1} for temperatures between 293 and 415 K, then increases abruptly by $\Delta\ \kappa_{th} =$ 0.22 W m^{-1} K^{-1} during the IMT. The electronic contribution to thermal conductivity ($k_{electronic}$) was calculated from the measured electrical conductivity using the Wiedemann–Franz law ($k_{electronic} = \sigma LT$), where σ is the conductivity, L is the Lorenz number ($L = 2.44 \times 10^{-8}$ WΩK^{-2}) and T is the temperature. As shown in Figure 1e, this represents a small contribution to the

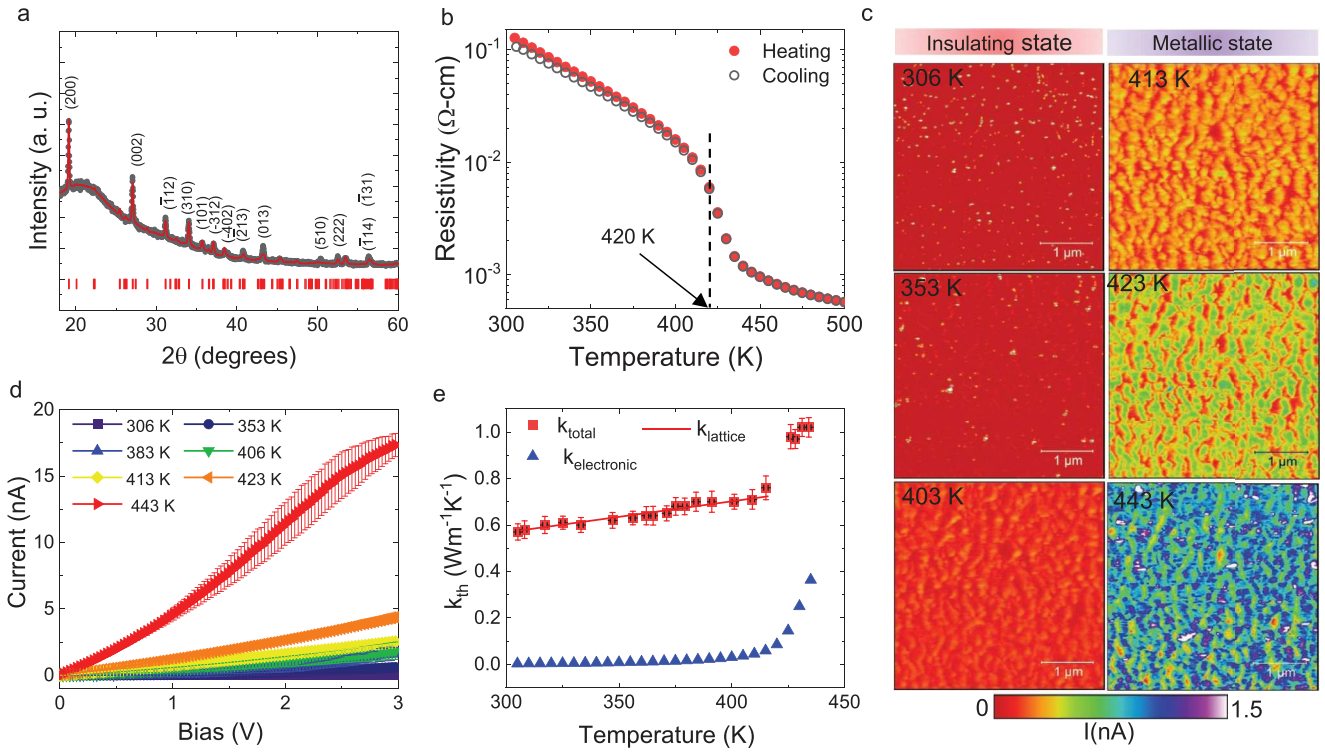

Figure 1. Material characterization of V_3O_5 film. a) Room-temperature XRD and Rietveld refinement for polycrystalline V_3O_5 films deposited on glass (SiO_2). b) Resistivity as a function of temperature in the range of 300–500 K for both heating and cooling cycles. The onset of the IMT is indicated as T_{IMT} at 420 ± 5 K. c) C-AFM images of V_3O_5 thin film on Pt substrate as a function of temperature with a bias 1 V. d) Temperature-dependent, multipoint *I–V* measurement. At high temperatures the *I–V* curve is linear while at the low temperature the *I–V* curve is non-linear, indicating the IMT in the V_3O_5 sample. e) Temperature-dependent thermal conductivity of V_3O_5 thin film measured by scanning near-field thermal microscopy using the 3ω-technique.

thermal conductivity of the insulating phase (i.e., <10%) but becomes more significant as the temperature approaches the IMT temperature, where it largely accounts for the increased thermal conductivity of the metallic phase. These data show that the thermal conductivity of the insulating phase is dominated by the lattice contribution which includes a broad range of phonon-scattering processes, including impurity scattering, phonon–phonon scattering, and grain-boundary scattering.[22] Under these conditions, the thermal conductivity has been shown to be well described by an empirical relationship of the form:[23]

$$k_{\text{lattice}} = a\left(\frac{T}{\theta_D}\right)^n \exp\left(\frac{\theta_D}{bT}\right) \quad (1)$$

where a, n, and b are constants and θ_D is the Debye temperature. A fit of this equation, using a Debye temperature for V_3O_5 of 444 K, is included in Figure 1e for the insulating phase. The fitting parameters were determined to form least squares fitting to be: a = 0.445, n = 1.5, and b = 1.8. Since the IMT in V_3O_5 is associated with a change in the arrangement of V^{3+} and V^{4+} ions within the monoclinic structure, it is not expected to have a significant effect on the lattice contribution to thermal conductivity.[14a,b] However, the room temperature thermal conductivity of our polycrystalline films is significantly lower (i.e., a factor of six) than that previously reported by Andreev et al. for bulk V_3O_5.[24]

2.2. Electroforming Free threshold Switching in V_3O_5

The electrical switching properties of V_3O_5-based MOM devices were studied using the experimental configuration shown in **Figure 2**a and typical results are shown in Figures 2b–f. When subjected to bidirectional voltage-sweeps the devices exhibit characteristic threshold switching, as illustrated in Figure 2b for a device in series with a 2 kΩ current-limiting resistor. As the voltage is ramped up to the "threshold" point (V_{th}, I_{th}), the device reverts to its low resistance state (ON-state) and when the voltage is subsequently ramped down below a second "hold" point (V_h, I_h) it reverts to its original high resistance state (OFF-state). Significantly, these devices exhibit threshold switching from the first ramping cycle and do not require an initial electroforming step to establish reliable switching. Under current-controlled operation, without a series resistor, the same device exhibits characteristic NDR, the onset of which coincides with the threshold point of the voltage-controlled characteristic measured without the load resistor.

Endurance testing using bipolar voltage sweeps over the range from +20 to −20 V shows that the threshold switching response is symmetric with respect to bias polarity and that it is particularly stable under repeated cycling (Figure 2c). This is more clearly shown in Figure 2d which plots the cycle-to-cycle threshold and hold voltages (after subtracting the voltage drop across the 2 kΩ resistor) for a device subjected to >10^4 voltage-controlled switching cycles. These data demonstrate

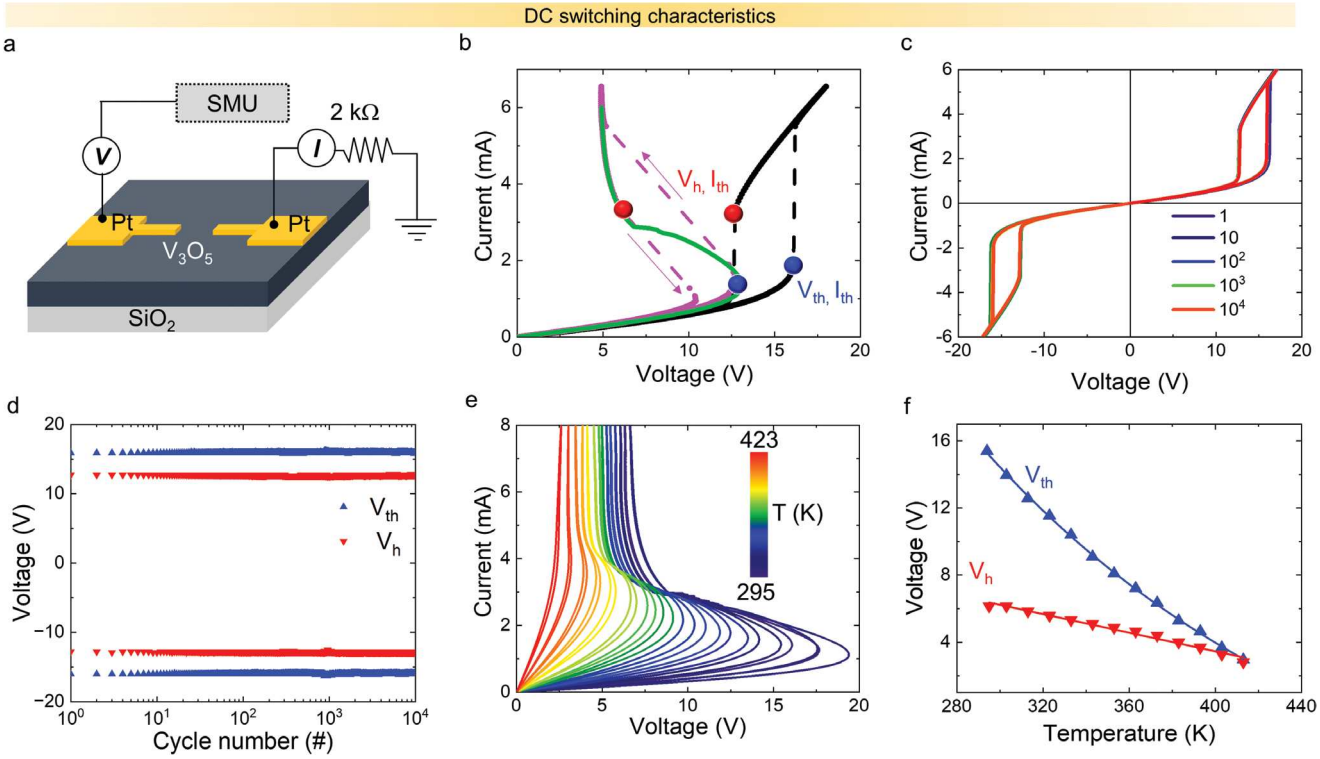

Figure 2. Quasi-static *I–V* characteristics of Pt/V_3O_5/Pt planar device. a) Schematic of the Pt/V_3O_5/Pt planar structure with electrical characterization setup. b) Quasi-static voltage-controlled *I–V* characteristics of a Pt/V_3O_5/Pt device (80 µm gap and 10 µm width) measured with a 2 kΩ series resistance (black line) and a pink line representing voltage drop against device resistance. The data series shown in green represents the current-controlled *I–V* characteristics of the same device. Blue points represent threshold points and red points represent hold points. c) DC endurance characteristics at room temperature with a 2 kΩ series resistance showing measured *I–V* characteristics after the specified number of cycles and d) cycle-to-cycle variability of threshold and hold voltages distribution for 10^4 dc cycles. e) NDR characteristic measured as a function of substrate temperature for the device with 80 µm gap and 10 µm width and f) temperature dependence of the threshold (V_{th}) and hold (V_h) voltage extracted from the *I–V* characteristic of the plot shown in (e).

a cycle-to-cycle variability of <3% in the threshold voltage and <0.5% in the hold voltage. It has previously been shown that variations in threshold voltage can originate from changes in device temperature during continuous dc cycling but no such effect is evident in the current study.[25] Subsequent analysis of the active device area using Raman spectroscopy confirmed that there was no permanent change in the crystal structure of the V_3O_5 after the endurance test (see Supporting Information), consistent with the low electric fields and operating temperatures associated with device operation.

Although individual devices show excellent switching reliability, the device-to-device variability was greater than expected for forming-free operation, with up to 10% variation in the threshold voltage and up to 12% variation in the hold voltage for devices of a given structure (see Supporting Information). This is at least partly attributable to the large grain size, roughness, and inhomogeneity of the functional V_3O_5 layers, which have increased significance for smaller-scale devices.

The threshold voltage was found to scale linearly with the electrode gap, with the onset of room-temperature switching occurring at a constant electric field of $\approx 2 \times 10^5$ V m^{-1} (see Supporting Information). On this basis it is tempting to refer to threshold switching as a field-initiated thermal run-away process. However, this is a misnomer, as switching does not depend explicitly on the electric field, only on the local temperature. This is evident from the data in Figure 2e which shows the NDR response of a V_3O_5 device heated to temperatures in the range from 293 to 423 K; These data show that V_{th} (threshold electric field) is not constant but decreases with increasing temperature, consistent with a thermal switching process. These temperature dependent measurements further show that both the threshold and hold voltages decrease with increasing device temperature, and that the NDR voltage window decreases due to the fact that the threshold voltage has a stronger temperature dependence than the hold voltage; increasing the substrate temperature by 100 K, from 295 to 413 K, causes a shift in the threshold voltage from V_{th} = 14.25 V to V_{th} = 2.41 V while the hold voltage varies from V_h = 4.99 V to V_h = 2.29 V. The NDR window disappears at a temperature of ≈415 K, consistent with the onset of the IMT in the V_3O_5 film. This is shown more explicitly in Figure 2f which shows V_{th} and V_h as a function of temperature, clearly showing their convergence at or near the IMT temperature.[26] At this point, the whole V_3O_5 films becomes conductive.

2.3. Origin of S-Type NDR in V_3O_5 Device

To gain further insight into the physical origins of the NDR in V_3O_5, Current–voltage (*I–V*) characteristics were correlated with

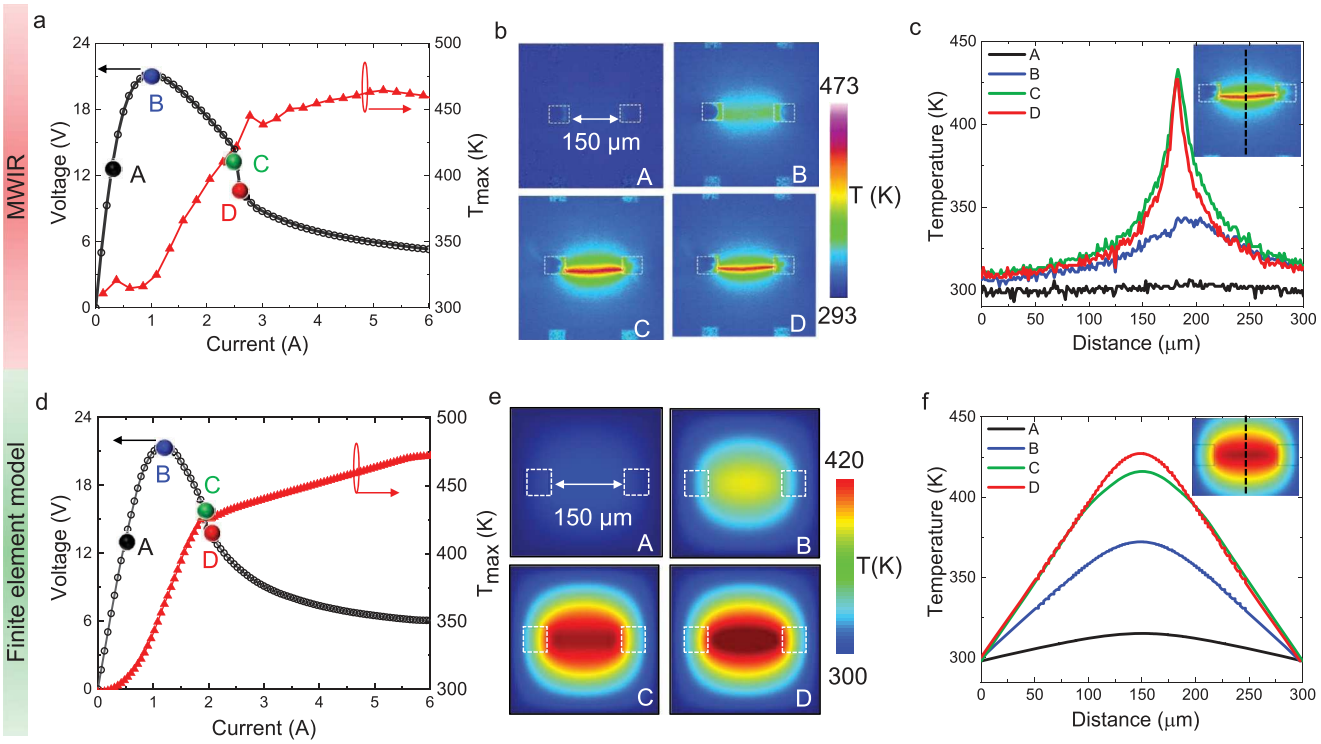

Figure 3. In situ temperature mapping and finite element modeling of S-type NDR in V_3O_5. a) In situ *I–V* characteristics of a Pt/V_3O_5/Pt device (electrode gap 150 μm and electrode width 50 μm) measured during in situ MWIR spectroscopy and the maximum temperature as a function of current. b) 2D map of temperature distribution of the device area for four distinct points (at A, B, C, and D points) as noted in (a) and c) corresponding line trace of temperature at the middle of the device vertically to the current flowing direction as marked in the inset. d) Simulated *I–V* characteristics with a maximum temperature of the device area as a function of applied current using finite element modeling, e) 2D plot of temperature at four different points (A, B, C, and D) marked in (d), and f) corresponding line trace of temperature at middle of the device vertically to the current flowing direction for the four different points marked in (d,e).

the temperature distributions caused by local Joule heating. **Figure 3**a compares the *I–V* characteristic and maximum local temperature measured in a device during a current scan from 0 to 6 mA, using current steps of 0.1 mA, and Figure 3b shows corresponding temperature maps at specific currents. These data clearly show that conduction is localized within a region much narrower than the electrode width and that the onset of NDR occurs at a temperature (≈320 K) well below the IMT temperature of V_3O_5 (425 K). Indeed, the local temperature only exceeds the IMT temperature at a current of 2.8 mA (i.e., point C), which is correlated with an abrupt change in the slope of the *I–V* characteristic (Figure 3a). The temperature maps also show that the current distribution becomes more localized at higher currents, as highlighted by the distributions in Figure 3c and by a plot of the full width at half maximum (FWHM) of the distribution as a function of current (see Supporting Information). This is a direct consequence of the fact that the conductivity of V_3O_5 film increases super-linearly with temperature.[16a] A further abrupt narrowing of the distribution is observed between points C and D, as the local temperature exceeds the V_3O_5 IMT temperature. This is accompanied by a slight decrease in the peak temperature due to a reduction in the static resistance of the device and the associated reduction in heating power (Joule heating) (see Supporting Information).

These results differ from the threshold switching behavior of VO_2-based devices, where the onset of NDR (i.e., V_{th}) coincides with the IMT and the associated structural phase transition.[27] However, they are similar to the behavior observed by Kumar et al.[27] in NbO_2-based devices, where a smooth S-type NDR region was followed by an abrupt snap-back region at higher currents attributed to the IMT transition in NbO_2, which occurs at 1080 K. While the change in the slope of the *I–V* characteristic at point C in Figure 3a is clearly associated with the V_3O_5 IMT, it also corresponds to a region of electrical oscillation (see Supporting Information). This is significant because Herzig et al.[28] have shown that instrumental averaging of such oscillations can produce an apparent change in slope similar to that observed. Although such an effect likely contributes to the change in slope in the present case, the data in Figure 3a–c are generally reproduced by a physics-based model based on the temperature-dependent conductivity V_3O_5. This suggests that this is the dominant influence on the *I–V* characteristics.

Physics-based modeling of the quasi-static response of V_3O_5-based devices was undertaken using a 2D finite element model to solve the electrical and thermal continuity equations for a metal/oxide/metal device structure and was undertaken using the COMSOL package (see Supporting Information for details). Results from the simulations are shown in Figure 3d–f and are in excellent qualitative agreement with the corresponding experimental data. The main difference is that the calculated temperature distributions are generally broader than the corresponding experimental distributions.

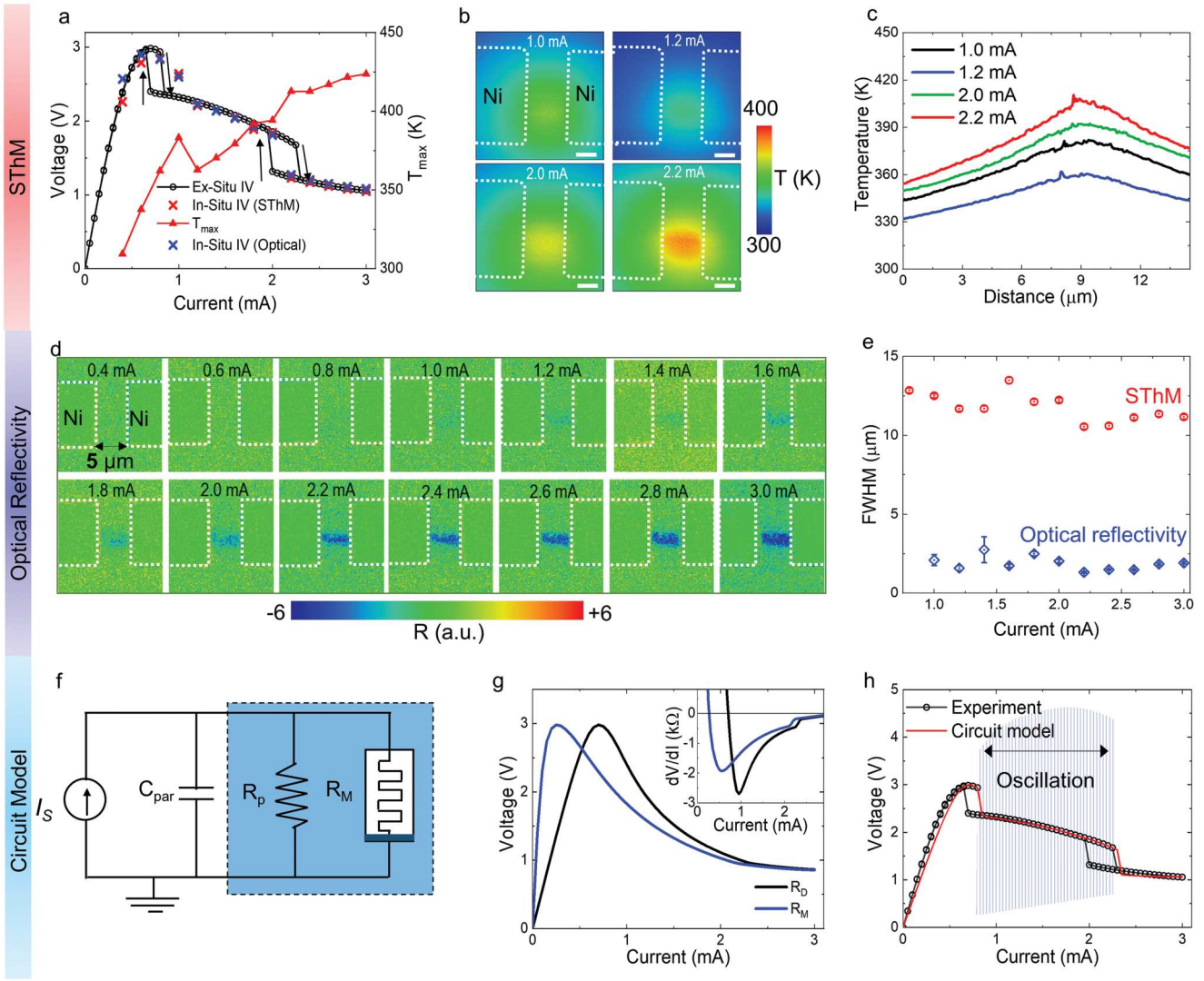

Figure 4. In situ SThM of multistep NDR in V_3O_5 device. a) In situ (SThM & optical reflectivity) and ex situ *I–V* characteristics of Ni/V_3O_5/Ni device (electrode gap 5 μm and electrode width 10 μm) and maximum temperature of the device area as a function of current, b) 2D SThM temperature map of the device area at four different current values (scale bar = 2 μm) and c) line trace of temperature in the device center for each current step measured. d) In situ 2D optical reflectivity map of the device area at different current values for the same device and e) FWHM of the optical reflectivity distribution and SThM temperature distribution as a function of applied current. f) Lumped-element circuit model for simulating the oscillating effect, g) simulated *I–V* characteristics without parasitic capacitance (C_{par} = 0, R_p = 6.7 kΩ) based on the circuit shown in (f), and h) simulated *I–V* characteristics of the memristor including the effect of parasitic capacitance (C_{par}= 35 pF, R_p = 6.7 kΩ).

The above results are in contrast to those of Adda et al.,[13] who showed that the filament temperature reaches the IMT temperature at the threshold point, with a sudden jump in local temperature. Instead, we observe a continuous current constriction throughout most of the NDR region, with a small, abrupt reduction in device power as the local temperature of the device reaches the IMT temperature of the V_3O_5 near the hold point.

2.4. Effect of Measurement-Induced Oscillations

In extending the study to smaller-scale devices (i.e., smaller electrode gaps), significant differences in the *I–V* characteristics were observed. This is immediately evident from a comparison of the CC-NDR characteristic in **Figure 4**a for a small device (5 μm electrode gap) and those in Figure 3a for a large device (150 μm electrode gap). While the large device exhibits continuous S-type NDR with an abrupt change in slope as the local temperature approaches the IMT temperature of V_3O_5, the small device exhibits abrupt, discontinuous voltage changes near both the threshold and hold points. The abrupt change at the threshold point occurs at a local temperature well below the IMT temperature and is followed by an apparent reduction in temperature at slightly higher currents, while that at the hold point (≈2.2 mA) coincides with the active region of the device reaching the IMT temperature of V_3O_5 (≈415 K).

Temperature mapping of these devices was undertaken using SThM and again showed that the current distribution

is limited to a region much narrower than the electrode width (Figure 4b). The FWHM of the temperature distribution at 1.0 mA is ≈12 μm and remains approximately constant for currents between the threshold and hold points (Figure 4c). Neither of the abrupt conductivity changes is accompanied by a corresponding localization of the temperature distribution. In contrast, the width of the temperature distribution in the larger device decreases from ≈90 to ≈20 μm over the current range between the threshold and hold points and undergoes abrupt localization as the temperature reaches the IMT temperature (Figure 3c).

The optical reflectivity of V_3O_5 has been shown to have a weak temperature dependence in its insulating and metallic states but to exhibit a decrease in reflectivity as it transitions between these states.[13] A decrease in reflectivity is therefore indicative of the IMT and can be used to map the distribution of the metallic phase. Figure 4d shows such maps for different device currents. A narrow region of lower reflectivity material becomes evident between the electrodes of the device as the current is increased beyond the hold point and becomes more evident with increasing current, consistent with a larger volume fraction of the V_3O_5 transitioning to the metallic state. However, the width of this region remains constant, with an FWHM of ≈2 μm, which is much narrower than the corresponding temperature distributions.

The abrupt voltage changes shown in Figure 4a are very similar to previously reported "snap-back" characteristics observed in NbO_x-based devices.[29] In that case, the effect was shown to result from an abrupt current bifurcation process in which the device current was concentrated from the surrounding device into a localized filamentary core. However, this is not the origin of the abrupt voltage changes in the present case. Indeed, more detailed analysis and lumped element modeling show that these abrupt changes originate from instrumental averaging of voltage oscillations.[28] As discussed above, this has previously been shown to account for apparent changes in the slope of the NDR characteristics. However, this is the first demonstration that it can also produce an apparent "snap-back" response.

To investigate the effect of voltage oscillation on the shape of the NDR region of the quasi-static *I–V* characteristics, we developed a circuit model of the device-under-test, as shown in Figure 4f. The V_3O_5 devices were modeled by a temperature-dependent memristor, which represents the conductive channel created by local Joule heating, and a parallel resistor, which accounts for conduction in the surrounding V_3O_5 film. The memristor model was adapted from that of Slesazeck et al.,[30] with the device resistance determined from a piecewise fit to the V_3O_5 resistivity–temperature data (see Supporting Information). The test circuit was completed by adding a parallel capacitor (C_{par}) to represent parasitic device and cable capacitances and the circuit response was simulated using LT-Spice. For a $C_{par} = 0$, the device does not oscillate and the resultant NDR is a smooth S-type characteristic as shown in Figure 4g. In contrast, the inclusion of a small parasitic capacitance results in device oscillation. For a parasitic capacitance of 35 pF, the voltage across the memristor starts oscillating as it is biased into the active NDR region of its DC *I–V* characteristics, as shown in Figure 4h. LT-Spice was used to time-average the device voltage in order to represent the averaging effect of the source-measurement unit employed for electrical testing. The resulting *I–V* characteristics were found to reproduce the two apparent "snap-back" regions observed experimentally (Figure 4h), clearly showing that such discontinuous *I–V* characteristics can be produced by processes other than the current bifurcation.[7a,29,31] Indeed, the parameters extracted from the present simulation do not meet the criterion for current bifurcation (i.e., $R_P < R_{NDR}$). For the case shown the maximum negative differential resistance (R_{NDR} = 1.83 kΩ) of the memristor alone is much lower than the magnitude of the parallel resistance (R_P = 6.7 kΩ) as shown inset in Figure 4g (the sensitivity of model parameters is included in the Supporting Information). The similarity between the abrupt voltage changes produced by instrumental averaging (Figure 4a) and those resulting from current bifurcation highlights the potential for misinterpreting such behavior and the importance of understanding the impact of the measurement system on device characteristics.

Electrical oscillation also explains the observed current-independent width of temperature distribution and the fact that the reflectivity distribution is much narrower than the temperature distribution (Figure 4); Electrical oscillation produces a corresponding variation in temperature so that the temperature distribution measured by SThM represents an average distribution. This implies that the measurements underestimate the peak temperature and explains why the measured distributions are insensitive to current confinement effects (see Supporting Information). As the device current increases, the peak temperature during oscillation will exceed the IMT temperature of V_3O_5, converting it into a metallic state. This gives rise to the observed increase in reflectivity and explains why the reflectivity distribution is narrower than that of the corresponding temperature distribution. The decrease in reflectivity with increasing current is a consequence of the increase in average temperature and oscillation frequency. Electrical oscillation can therefore account for both the observed electrical characteristics and the corresponding thermal response of these devices.

2.5. Oscillation Dynamics of Single and Coupled Oscillators

To verify the functionality of V_3O_5 memristors as relaxation oscillators we studied the dynamics of single and coupled devices. **Figure 5**a shows the NDR characteristics of a Pt/V_3O_5/Pt device (D#1 -Electrodes: 10 μm gap and 10 μm width), together with the Pearson-Anson oscillator circuit employed to test the oscillator response. Figure 5b shows the corresponding oscillator response as a function of applied voltage, using an external parallel capacitor of 20 nF and a 2.5 kΩ load resistance. Self-oscillation is triggered for a minimum voltage of 8.3 V, which results in an oscillation frequency of 7.08 kHz at room temperature. The oscillation frequency increases with increasing source voltage, as shown in Figure 5c; Damped oscillations are observed when the source voltage is close to the upper limit of the oscillation window. The increase in oscillation frequency is attributed to a reduction in device resistance and is consistent with the frequency relation:[32]

$$\tau_o = \tau_r \ln\left(\frac{V_S - V_{th}}{V_S - V_h}\right) + \tau_f \ln\left(\frac{V_S - V_h}{V_S - V_{th}}\right) \quad (2)$$

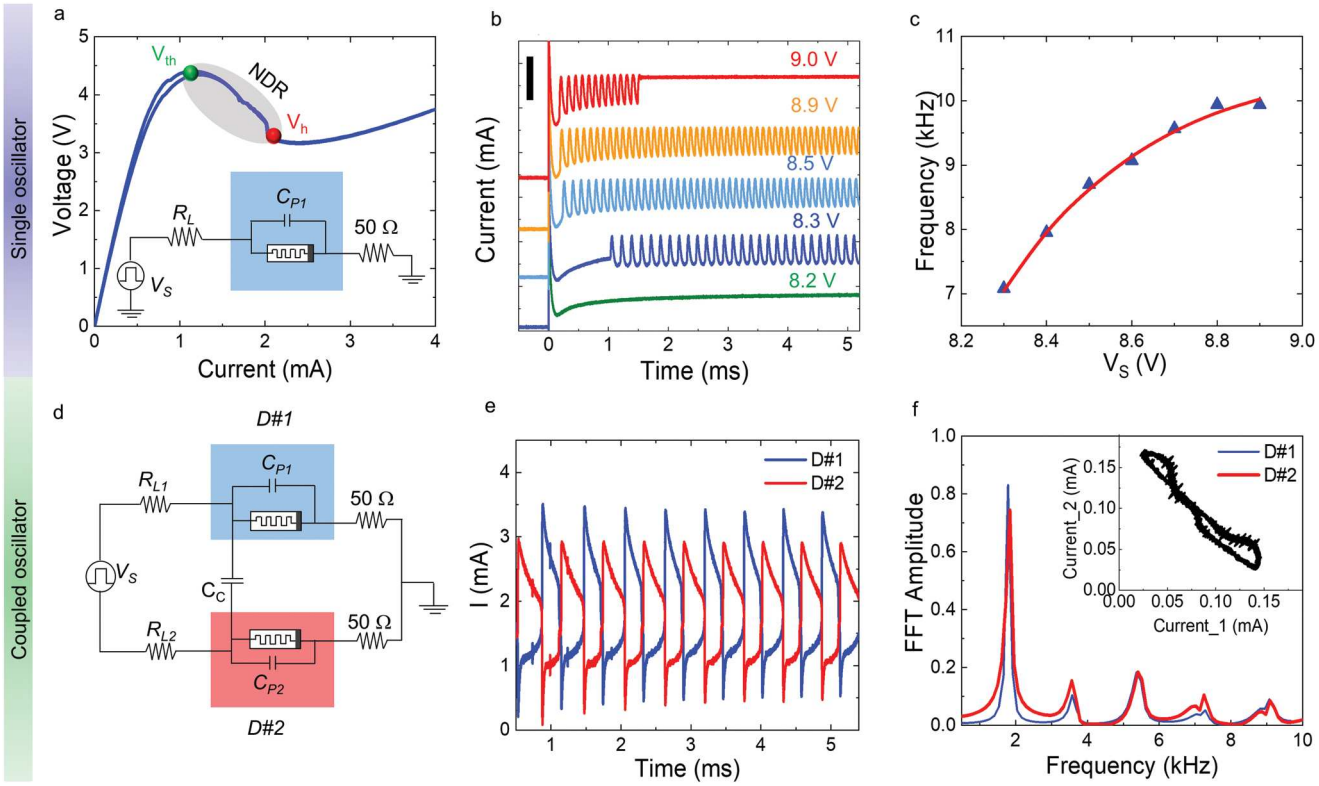

Figure 5. Oscillation dynamics of single and coupled oscillators. a) NDR characteristics of a device (10 µm gap and 10 µm width) with a schematic of the circuit diagram for a single oscillator in the inset. b) Oscillation characteristics for an individual oscillator for different applied bias with $R_L = 2.5$ kΩ and $C_p = 20$ nF. The scale represents 1 mA. c) Corresponding oscillation frequency of the oscillator as a function of applied bias. d) A schematic circuit diagram for capacitively coupled oscillators. e) Device currents for an 8.3 V voltage pulse coupled with $R_{L1} = 2.5$ kΩ, $R_{L2} = 3$ kΩ and $C_C = 1$ nF. f) Corresponding FFT amplitude spectra of the coupled oscillators. The inset shows a current phase-space diagram of the coupled oscillators.

where $\tau_{r,f} = C(R_L \| R_{ins,met})$, with $C = (C_i + C_{cp1})$ the sum of intrinsic and external capacitances, $R_{ins,met}$ the maximum (insulating) and minimum (metallic) resistance values of the V_3O_5 device, V_{th} and V_h the threshold and hold voltages. The solid lines in Figure 5c represent a fit of this equation to the data (see Supporting Information for fitting details). No variation in the oscillation frequency was observed during five repeated operation cycles indicating a stable NDR characteristic and a promising candidate for building stable solid-state neurons. A comparison of the spiking characteristics of V_3O_5 with that of other candidates (i.e., VO_2, NbO_2) is presented in **Table 1**. It is important to note that the threshold voltage and current scale with device size (see Supporting Information). As such, device scaling will be important for achieving low power threshold switching.

Table 1. Comparison of various memristor-based neurons.

Structure	Device structure	Frequency	Energy/spike	Reference
Au/VO_2/Au	planar	400–1300 kHz	130–340 nJ	[33]
Au/VO_2/Au	planar	5–11.4 kHz	≈950 nJ	[34]
Pt/VO_2/Pt	planar	7.5–20 kHz	100–250 µJ	[2b]
Pt/VO_2/Pt	cross-point	16.8–61 kHz	0.5–4 nJ	[13]
Pt/NbO_2/Pt	cross-point	10–40 kHz	2–10 µJ	[27]
Pt/Ti/NbOx/Pt	cross-point	2–20 MHz	≈150 pJ	[35]
Pt/Ti/Ti: Nb_2O_5/Pt	cross-point	12–25 MHz	170–330 pJ	[36]
Au/V_3O_5/Au	planar	0.7–20 kHz	25–1000 µJ	[13]
Pt/V_3O_5/Pt	planar	3–630 kHz	17 nJ–2.6 µJ	This work

The application of relaxation oscillators in analog computing is enabled by their rich coupling dynamics[37] To investigate such behavior, we coupled two dissimilar oscillators (D#1 and D#2, see Supporting Information) with a capacitor (C_C) as summarized in Figure 5d. The coupled responses for D#1 and D#2 were monitored by measuring the voltage drop across a 50 Ω resistor in series with each device. Variations in the coupling parameters (e.g., V_S, C_p and C_C) cause changes in the frequency and phase difference of the oscillators due to their mutual interaction. The synchronization dynamics of this coupled oscillatory system shows frequency and phase locking, eventually converging to a single resonant frequency with in-phase and out-of-phase locking. In a capacitively coupled system, the coupling capacitance modifies the frequency dynamics of the individual oscillators.[38] For a coupling capacitance larger than 1 nF, the synchronized oscillations depend on the bias and parasitic capacitances of devices D#1 and D#2 (see Supporting Information for details). For example, when the input voltage is 8.3 V both oscillators and the self-coupling elements are $R_{L1} = 2.5$ kΩ, $R_{L2} = 3$ kΩ, $C_P = 20$ nF and $C_C = 20$ nF lead to out-of-phase (180° phase) oscillation. The underlying dynamics are such that when device D#1 switches from a metallic-state

to an insulating-state, device D#2 concurrently transits from an insulating-state to a metallic-state, producing a 180° phase relationship in device current between the two oscillators. Fast Fourier Transform (FFT) spectra of the coupled oscillators show that both devices have a unique synchronized frequency of 1.8 kHz, which is much lower than that of the individual oscillators in this case as presented in Figure 5c. The experimentally observed frequency locking behavior is also verified through circuit simulations using lumped element modeling. This synchronization behavior is consistent with VO_2-and NbO_2-based capacitively coupled oscillators.[1c,37a,39]

3. Conclusion

The structural, electrical, and thermal properties of polycrystalline V_3O_5 films have been reported, together with their as the functional oxide layer in metal/oxide/metal relaxation oscillators. V_3O_5-based devices were shown to exhibit reliable, forming-free threshold-switching and current-controlled NDR, with representative devices showing <3% variation in V_{th} and <0.5% variation in V_h over 10^4 switching cycles. Conduction in lateral-device structures was confined to a narrow filamentary path due to the self-confinement of the current in response to the increase in film conductivity created by local Joule heating. Device-to-device variability was greater than expected for forming-free operation, with up to 10% variation in V_{th} and 12% variation in V_h for devices of a given structure. However, much of this was attributed to film roughness that resulted from the large and inhomogeneous grain size of the V_3O_5 film. The threshold and hold voltages were shown to decrease with increasing device temperature, with an NDR window maintained up to the V_3O_5 IMT temperature (i.e., ≈415 K), which is much higher than that achievable with VO_2.

The NDR characteristics of in-plane devices were found to depend on the electrode geometry due to changes in the magnitude of the device resistance and NDR, with larger devices exhibiting smooth S-type NDR characteristics and smaller devices exhibiting more complex snap-back-like characteristics similar to those previously reported for NbO_x-based devices.[29] The S-type NDR response of larger devices was shown to result from the strong temperature dependence of the insulating phase of V_3O_5 and to occur at a temperature well below the IMT temperature, while the apparent "snap-back" characteristics of the smaller devices were shown to be a consequence of measurement-induced electrical oscillations. This understanding was achieved by comparing measured electrical and thermal characteristics with device simulations based on finite-element and lumped-element device models.

Finally, we demonstrated the functionality of individual and coupled V_3O_5-based relaxation oscillators, including fast-spiking of individual oscillators similar to that of VO_2 and NbO_2 devices, and frequency and phase-locking of coupled devices, as required for oscillator-based computing.

These studies have clearly demonstrated the potential of V_3O_5 as a function oxide and paved the way for further development of threshold switching and oscillator-based neuromorphic computing devices. They have also highlighted the importance of understanding the influence of the measurement system on device characteristics and the potential for misinterpreting specific characteristics.

4. Experimental Section

Thin film Deposition: V_3O_5 thin films were grown on glass (SiO_2) substrates by pulsed direct-current (DC) magnetron sputtering of a vanadium (99.95% pure) target in a reactive Ar/O_2 ambient. The substrate was held at a temperature of 873 K during deposition and the ambient pressure was maintained at 1.3 Pa using Ar/O_2 flow rates of 195/5.5 sccm. The sample was located 10 cm from the sputter target and the pulsed DC sputtering power was 150 W. Similar films were also deposited on Pt-coated SiO_2 substrates to enable through-film electrical characterization.

Structural and Physical Characterization: The structure, composition, and morphology of the films were subsequently analyzed using grazing-incidence X-ray diffraction (GI-XRD), XPS, atomic force microscopy (AFM) (Bruker), and scanning electron microscopy. Through-film current mapping was undertaken with a conducting AFM, (Asylum research) using a scanning frequency of 1 Hz and a contact force of 62 nN. Measurements of thermal conductivities were performed by SThM, using the so-called 3ω-technique.[21] The technique was based on atomic force microscopy using a resistive thermal probe (Bruker Vita-SThM) that was electrically powered with a frequency between 3 and 7 kHz. More details of the SThM system can be found in ref. [40]. The SThM was integrated into the analysis chamber of an environmental scanning electron microscope, which allowed the selection of the region of interest by electron microscopy and concomitant analysis of the thermal properties by SThM under vacuum conditions.

Device Fabrication: Planar, two-terminal MOM device structures were fabricated by depositing 200 nm Pt or 200 nm Ni electrode layers on top of the V_3O_5 film. The electrodes were defined using a lift-off process based on electron beam lithography, and the metal layers were deposited by e-beam evaporation using a 5 nm Ti adhesion layer. The final electrodes were 10–50 µm wide and separated by gaps in the range 5–150 µm.

Electrical Characterization: Ex situ electrical characterization was performed using an Agilent B1500A semiconductor parametric analyzer attached to a Signatone probe station with a heating stage. Quasi-static *I–V* characteristics were measured under voltage- and current-controlled operation, for temperature in the range 295–423 K. The sample stage was held at temperature for 5 mins prior to each measurement to stabilize the device temperature. During voltage sweeps the current was limited by a series resistor or instrumental compliance current to prevent permanent device damage (or structural change).

Oscillator dynamics were also measured using a simple Pearson-Anson oscillator circuit. In this case, a Rigol MSO-8104 4-channel digital oscilloscope was used to monitor the voltage drop across the 50 Ω monitor resistor in series with the device. In situ thermal imaging of the devices during electrical testing was undertaken using either an InfraScope MWIR temperature mapping microscope employing by an InSb detector (Quantum Focus Instruments Co.)[41] or SThM mapping using an SThM probe (VITA-DM-GLA from Brucker probes) mounted in a Dimension 3100 AFM.[42] The former had a spatial resolution of ≈3 µm, while the latter had a resolution of ≈100 nm. Thermal imaging was complemented by in situ optical reflectivity mapping of the device.

Statistical Analysis: Rietveld refinement was used to determine the positions, heights, and widths of XRD peaks. The authors used Pseudo-Voigt functions to fit the data based on χ^2 minimization using the Fullprof software package. Threshold and hold voltages were determined from the mean and standard deviation of measurements performed on ten devices for each device size. The uncertainty in the absolute value of the thermal conductivity represented the standard deviation of at least 15-line measurements over a length of 8 µm using a resolution of 250 measuring points. It originated from calibration uncertainties, including the absolute value used for the thermal conductivity of the reference

material. The relative change in thermal conductivity with temperature was less prone to error, with the uncertainty determined from the correlation coefficients of the resulting $U_{3\omega}$ versus ln ω slopes.

Supporting Information

Supporting Information is available from the Wiley Online Library or from the author.

Acknowledgements

The authors would like to acknowledge the access to NCRIS facilities at the ACT node of the Australian National Fabrication Facility (ANFF) and the Heavy-Ion Accelerator Capability (HIA). The authors also acknowledge the facilities, and the scientific and technical assistance of the Australian Microscopy & Microanalysis Research Facility at the Centre of Advanced Microscopy, ANU. A.R. and C.V. gratefully acknowledge the support from the National Science Foundation, Award No. 2033328. This work was also partly funded by the Lyon Institute of Nanotechnologies (INL) in the framework of the BQRi 2021 project "Team BabAlbPuy". S.K.Nath acknowledges the support of the Forrest Prospect Fellowship awarded by the Forrest Research Foundation, Australia. The authors would also like to thank Dr. Christian Notthoff for the Raman analysis. The authors also acknowledge the access to XPS facilities and scientific and technical assistance at the Surface Analysis Laboratory at the Mark Wainwright Analytical Centre, The University of New South Wales, Sydney. T.L. and Y.L. acknowledge the support of the ARC Discovery Project (DP200100159) and the Laurate Fellowship Program (FL210100017). T.H., R.H., and T.Riedl acknowledge the support of the Deutsche Forschungsgemeinschaft (DFG) under project numbers HE 2698/11-1.

Open access publishing facilitated by Australian National University, as part of the Wiley - Australian National University agreement via the Council of Australian University Librarians.

Conflict of Interest

The authors declare no conflict of interest.

Author Contributions

S.K.Nandi was responsible for the overall direction and planning of the project. S.K.D. and S.K.Nandi carried out the device fabrication, electrical characterization, data analysis, numerical simulations and drafted the initial manuscript. R.G.E. contributed to data interpretation and RBS analysis, developed the finite-element and circuit models, and edited and revised the manuscript. C.V.M. and A.R. deposited V_3O_5 thin films and performed XRD and resistivity measurements. M.U. characterized the in situ temperature mapping by mid-wave infrared (MWIR) spectroscopy. E.P., D.A., and N.B. performed the in situ scanning thermal microscopy (SThM) and optical reflectivity measurements of the devices. T.L. and Y.L. undertook the temperature-dependent conducting atomic force microscopy (C-AFM) measurements. T.H., R.H., and T.Riedl performed the thermal conductivity measurements by scanning near-field thermal microscopy (SThM) using the 3ω-technique. T.Ratcliff contributed to Rutherford backscattering analysis. S.K.Nath aided in material characterization. All the authors discussed the results and contributed to the final manuscript.

Data Availability Statement

The data that support the findings of this study are available from the corresponding author upon reasonable request.

Keywords

metal–insulator transition, negative differential resistance, neuromorphic computing, threshold switching, V_3O_5

Received: September 15, 2022
Revised: November 28, 2022
Published online: December 30, 2022

[1] a) S. Kumar, J. P. Strachan, R. S. Williams, *Nature* **2017**, *548*, 318; b) S. K. Nandi, X. Liu, D. K. Venkatachalam, R. G. Elliman, *J. Phys. D: Appl. Phys.* **2015**, *48*, 195105; c) S. Li, X. Liu, S. K. Nandi, D. K. Venkatachalam, R. G. Elliman, *Nanotechnology* **2017**, *28*, 125201; d) A. Mehonic, A. J. Kenyon, *Nature* **2022**, *604*, 255.

[2] a) M. D. Pickett, G. Medeiros-Ribeiro, R. S. Williams, *Nat. Mater.* **2013**, *12*, 114; b) W. Yi, K. K. Tsang, S. K. Lam, X. Bai, J. A. Crowell, E. A. Flores, *Nat. Commun.* **2018**, *9*, 4661.

[3] a) M. Belyaev, A. Velichko, *Electronics* **2019**, *8*, 1065; b) S. R. Kulkarni, A. V. Babu, B. Rajendran, in *2017 IEEE 60th Int. Midwest Symp. on Circuits and Systems (MWSCAS)*, IEEE, Piscataway, NJ, USA **2017**, pp. 426–431; c) J. L. Andrews, D. A. Santos, M. Meyyappan, R. S. Williams, S. Banerjee, *Trends Chem.* **2019**, *1*, 711; d) D. Joksas, E. Wang, N. Barmpatsalos, W. H. Ng, A. J. Kenyon, G. A. Constantinides, A. Mehonic, *Adv. Sci.* **2022**, *9*, 2105784.

[4] a) E. Corti, J. A. Cornejo Jimenez, K. M. Niang, J. Robertson, K. E. Moselund, B. Gotsmann, A. M. Ionescu, S. Karg, *Front. Neurosci.* **2021**, *15*, 628254; b) N. Shukla, A. Parihar, M. Cotter, M. Barth, X. Li, N. Chandramoorthy, H. Paik, D. G. Schlom, V. Narayanan, A. Raychowdhury, in *2014 IEEE Int. Electron Devices Meeting*, IEEE, Piscataway, NJ, USA **2014**, https://doi.org/10.1109/IEDM.2014.7047129.

[5] G. A. Gibson, *Adv. Funct. Mater.* **2018**, *28*, 1704175.

[6] S. K. Nandi, X. Liu, D. K. Venkatachalam, R. G. Elliman, *Appl. Phys. Lett.* **2015**, *107*, 132901.

[7] a) J. M. Goodwill, G. Ramer, D. Li, B. D. Hoskins, G. Pavlidis, J. J. McClelland, A. Centrone, J. A. Bain, M. Skowronski, *Nat. Commun.* **2019**, *10*, 1628; b) V. Malinenko, A. Pergament, O. Spirin, V. Nikulshin, *J. Sel. Top. Nano Electron. Comput.* **2014**, *2*, 45.

[8] D. Li, A. A. Sharma, N. Shukla, H. Paik, J. M. Goodwill, S. Datta, D. G. Schlom, J. A. Bain, M. Skowronski, *Nanotechnology* **2017**, *28*, 405201.

[9] a) X. Gao, C. M. M. Rosário, H. Hilgenkamp, *AIP Adv.* **2022**, *12*, 015218; b) S. K. Nandi, S. K. Das, C. Estherby, A. Gentle, R. G. Elliman, *J. Appl. Phys.* **2020**, *128*, 244103; c) K. Kosuge, *J. Phys. Soc. Jpn.* **1967**, *22*, 551.

[10] J. Srinivasan, S. V. Adve, P. Bose, J. A. Rivers, *ACM SIGARCH Computer Architecture News* **2004**, *32*, 276.

[11] a) A. Moatti, R. Sachan, V. R. Cooper, J. Narayan, *Sci. Rep.* **2019**, *9*, 3009; b) V. Balakrishnan, C. Ko, S. Ramanathan, *J. Mater. Res.* **2012**, *27*, 1476.

[12] a) J. A. Rupp, M. Querré, A. Kindsmüller, M.-P. Besland, E. Janod, R. Dittmann, R. Waser, D. J. Wouters, *J. Appl. Phys.* **2018**, *123*, 044502; b) T. Hennen, D. Bedau, J. Rupp, C. Funck, S. Menzel, M. Grobis, R. Waser, D. Wouters, in *2019 IEEE 11th Int. Memory Workshop (IMW)*, IEEE, Piscataway, NJ, USA **2019**, https://doi.org/10.1109/IMW.2019.8739556.

[13] C. Adda, M.-H. Lee, Y. Kalcheim, P. Salev, R. Rocco, N. M. Vargas, N. Ghazikhanian, C.-P. Li, G. Albright, M. Rozenberg, *Phys. Rev. X* **2022**, *12*, 011025.

[14] a) V. Andreev, V. Klimov, *Phys. Solid State* **2011**, *53*, 2424; b) F. Chudnovskii, E. Terukov, D. Khomskii, *Solid State Commun.* **1978**, *25*, 573; c) C. Aguilar-Maldonado, E. Solana-Madruga, C. Ritter, O. Mentré, A. M. Arevalo-Lopez, *Chem. Mater.* **2022**, *34*, 5294.

[15] E. I. Terukov, F. A. Chudnovskii, W. Reichelt, H. Oppermann, W. Brückner, H. P. Brückner, W. Moldenhauer, *Phys. Status Solidi A* **1976**, *37*, 541.
[16] a) A. Rúa, R. D. Díaz, N. Kumar, S. Lysenko, F. E. Fernández, *J. Appl. Phys.* **2017**, *121*, 235302; b) M.-H. Lee, Y. Kalcheim, J. d. Valle, I. K. Schuller, *ACS Appl. Mater. Interfaces* **2020**, *13*, 887.
[17] B. Fisher, L. Patlagan, K. Chashka, C. Makarov, G. Reisner, *Appl. Phys. Lett.* **2016**, *109*, 103501.
[18] N. Kumar, A. Rúa, J. Lu, F. Fernández, S. Lysenko, *Phys. Rev. Lett.* **2017**, *119*, 057602.
[19] D. Chen, H. Tan, X. Rui, Q. Zhang, Y. Feng, H. Geng, C. Li, S. Huang, Y. Yu, *InfoMat* **2019**, *1*, 251.
[20] B. T. O'callahan, A. C. Jones, J. Hyung Park, D. H. Cobden, J. M. Atkin, M. B. Raschke, *Nat. Commun.* **2015**, *6*, 6849.
[21] D. G. Cahill, *Rev. Sci. Instrum.* **1990**, *61*, 802.
[22] H. Kizuka, T. Yagi, J. Jia, Y. Yamashita, S. Nakamura, N. Taketoshi, Y. Shigesato, *Jpn. J. Appl. Phys.* **2015**, *54*, 053201.
[23] J. M. Ziman, *Electrons and Phonons: The Theory of Transport Phenomena in Solids*, Oxford University Press, Oxford, UK **2001**.
[24] V. Andreev, F. Chudnovskij, A. Petrov, E. Terukov, *Phys. Status Solidi A* **1978**, *48*, K153.
[25] S. B. Lee, K. Kim, J. S. Oh, B. Kahng, J. S. Lee, *Appl. Phys. Lett.* **2013**, *102*, 063501.
[26] V. Andreev, F. Chudnovskii, *J. Eng. Phys.* **1975**, *28*, 609.
[27] S. Kumar, M. D. Pickett, J. P. Strachan, G. Gibson, Y. Nishi, R. S. Williams, *Adv. Mater.* **2013**, *25*, 6128.
[28] M. Herzig, M. Weiher, A. Ascoli, R. Tetzlaff, T. Mikolajick, S. Slesazeck, *J. Phys. D: Appl. Phys.* **2019**, *52*, 325104.
[29] a) S. Li, X. Liu, S. K. Nandi, S. K. Nath, R. Elliman, *Adv. Funct. Mater.* **2019**, *29*, 1905060; b) S. K. Nandi, S. K. Nath, A. E. El-Helou, S. Li, X. Liu, P. E. Raad, R. G. Elliman, *Adv. Funct. Mater.* **2019**, *29*, 1906731.
[30] S. Slesazeck, H. Mähne, H. Wylezich, A. Wachowiak, J. Radhakrishnan, A. Ascoli, R. Tetzlaff, T. Mikolajick, *RSC Adv.* **2015**, *5*, 102318.
[31] S. Kumar, Z. Wang, N. Davila, N. Kumari, K. J. Norris, X. Huang, J. P. Strachan, D. Vine, A. D. Kilcoyne, Y. Nishi, *Nat. Commun.* **2017**, *8*, 658.
[32] E. Corti, B. Gotsmann, K. Moselund, A. M. Ionescu, J. Robertson, S. Karg, *Solid-State Electron.* **2020**, *168*, 107729.
[33] Y. Ma, P. P. Yeoh, L. Shen, J. M. Goodwill, J. A. Bain, M. Skowronski, *J. Appl. Phys.* **2020**, *128*, 194501.
[34] M. Pattanayak, M. N. F. Hoque, Z. Fan, A. A. Bernussi, *Sci. Technol. Adv. Mater.* **2018**, *19*, 693.
[35] M. G. Burzo, P. L. Komarov, P. E. Raad, *IEEE Trans. Compon. Packag. Technol.* **2005**, *28*, 637.
[36] S. K. Nath, S. K. Nandi, T. Ratcliff, R. G. Elliman, *ACS Appl. Mater. Interfaces* **2021**, *13*, 2845.
[37] a) A. Mallick, M. K. Bashar, D. S. Truesdell, B. H. Calhoun, S. Joshi, N. Shukla, in *2021 IEEE Int. Symp. on Circuits and Systems (ISCAS)*, IEEE, Piscataway, NJ, USA **2021**, https://doi.org/10.1109/ISCAS51556.2021.9401188; b) A. Ascoli, M. Weiher, R. Tetzlaff, M. Herzig, S. Slesazeck, T. Mikolajick, in *2021 10th Int. Conf. on Modern Circuits and Systems Technologies (MOCAST)*, IEEE, Piscataway, NJ, USA **2021**, https://doi.org/10.1109/MOCAST52088.2021.9493418; c) A. Ascoli, M. Weiher, M. Herzig, S. Slesazeck, T. Mikolajick, R. Tetzlaff, *J. Low Power Electron. Appl.* **2022**, *12*, 22; d) A. Parihar, N. Shukla, M. Jerry, S. Datta, A. Raychowdhury, *Sci. Rep.* **2017**, *7*, 911.
[38] N. Shukla, A. Parihar, E. Freeman, H. Paik, G. Stone, V. Narayanan, H. Wen, Z. Cai, V. Gopalan, R. Engel-Herbert, *Sci. Rep.* **2014**, *4*, 1.
[39] a) N. Shukla, S. Datta, A. Parihar, V. Narayanan, A. Raychowdhury, in *CNNA 2016; 15th Int. Workshop on Cellular Nanoscale Networks and their Applications*, IEEE, Piscataway, NJ, USA **2016**, pp. 1–2; b) D. Lee, E. Cha, J. Park, C. Sung, K. Moon, S. A. Chekol, H. Hwang, *IEEE J. Electron Devices Soc.* **2018**, *6*, 250.
[40] T. Haeger, M. Ketterer, J. Bahr, N. Pourdavoud, M. Runkel, R. Heiderhoff, T. Riedl, *J. Phys. Mater.* **2020**, *3*, 024004.
[41] a) M. Uenuma, Y. Ishikawa, Y. Uraoka, *Appl. Phys. Lett.* **2015**, *107*, 073503; b) S. K. Nandi, S. K. Nath, A. E. El-Helou, S. Li, T. Ratcliff, M. Uenuma, P. E. Raad, R. G. Elliman, *ACS Appl. Mater. Interfaces* **2020**, *12*, 8422.
[42] S. K. Nandi, E. Puyoo, S. K. Nath, D. Albertini, N. Baboux, S. K. Das, T. Ratcliff, R. G. Elliman, *ACS Appl. Mater. Interfaces* **2022**, *14*, 29025.